17B.1 The Dynamical Influences of Cloud Shading on Simulated Supercell Thunderstorms

JEFFREY FRAME*, PAUL MARKOWSKI, AND JONATHAN PETTERS

Department of Meteorology, Pennsylvania State University, University Park, PA

1. Introduction

Supercell thunderstorms have been among the most simulated atmospheric phenomena of the past three decades, owing to their societal impact (e.g., Brooks et al. 1994) and their often observed relatively steady behavior. Since three-dimensional numerical modeling of deep moist convection became computationally tractable in the late 1970s, scores of studies have aimed to further the understanding of the dynamics of supercell thunderstorms. To the authors' knowledge, no previous modeling study has sought to identify the potential dynamical effects of radiative transfer on supercell thunderstorms. Various reasons have been given for this, including computational expediency, the assumption that radiative processes are not as important as other convective-scale processes (Trier et al. 1997, 1998), and that convective storms are "largely dynamically, (not radiatively) driven" (Finley et al. 2001). Of the prior investigations that included radiative processes, most were two-dimensional simulations of mesoscale convective systems (MCSs) that focused on longwave radiation only (e.g., Miller and Frank 1993; Chin 1994; Xu and Randall 1995). Radiation has also been included in some simulations of cumulus convection (e.g., Khairoutdinov and Randall 2002, 2003), but its dynamical effects have not been systematically examined, especially on supercells.

Observations have confirmed that the extinction of the direct solar beam by the anvil clouds of supercell thunderstorms can cause a dramatic reduction in the net radiative flux at the surface in as little as 15 minutes (Markowski et al. 1998), leading to air temperature deficits of approximately 3 K beneath the anvils. Dowell and Bluestein (1997) observed a gradual 5 K temperature decrease between full sun and the onset of light precipitation in instrumented tower measurements of another supercell thunderstorm. Since this temperature drop was gradual, it was likely that the total temperature decrease was not caused by the passage of a gust front or other atmospheric boundary over the instrumented tower. These cases at least suggest that these particular supercell thunderstorms modified their environments via the extinction of shortwave radiation. Given that most supercell thunderstorms occur during the late afternoon and early evening hours (e.g., Kelly et al. 1978), it is suspected that radiation may similarly modify the near-storm environments of other supercells.

A pair of numerical simulations of supercell thunderstorms performed by Markowski and Harrington (2005) revealed that parameterized surface radiative cooling coupled with a surface sensible heat flux led to large changes in simulated mesocyclone strength. The emulated radiative cooling was admittedly crude; a constant prescribed cooling rate of 6 K h^{-1} was applied to any surface grid point at which cloud was overhead. It was stressed in that paper that the size of the anvil was likely underdone because the simulations only considered warm-rain (Kessler 1969) processes and, thus, the anvil likely did not spread as far downwind as it would have had ice microphysics been used. Nevertheless, that study demonstrated that the inclusion of radiative processes in supercell simulations could significantly modify the near-storm environment through the creation of a mass of radiatively cooled air beneath the anvil.

Supercell thunderstorms were chosen for this study because they have been extensively studied and are relatively isolated, long-lived, and steady-state compared to other forms of deep moist convection. Ordinary convection and multicellular convection, for example, exhibit updrafts and rotational characteristics that are much more transient than those of supercells. Additionally, observations have shown that interactions between convective cells are far more common for ordinary and multicellular storms, which limits the reproducibility of simulations of those convective modes when compared to supercells. Section 2 describes the model setup and methodology, section 3 contains a summary of the results, and section 4 presents the conclusions and suggestions for future work.

2. Model description and methodology

The Atmospheric Regional Prediction System (ARPS) model, version 5.1.5 (Xue et al. 2000, 2001) was employed for all simulations. Simulations were run on a grid that is 160 km in the east-west direction (x), 150 km in the north-south direction (y), and 18 km in the vertical direction (z). Care was taken so that the leading edge of the anvil would not move out of the domain. Open radiation boundary conditions are imposed at all lateral boundaries as described by Orlanski (1976). A rigid lid exists at the top of the domain with a Rayleigh sponge layer beneath it to absorb vertically-propagating gravity waves. The simulations employ a horizontal grid spacing of 1 km. The vertical grid is a stretched grid with an average spacing of 500 m and a minimum spacing of 50 m near the surface. Fourth-order numerical diffusion was employed to remove the spurious $2\Delta x$ and $4\Delta x$ waves that develop as a result of the leapfrog advection schemes within ARPS. A six-species cloud microphysics package was used (Lin et al. 1983) with adjustments made by Tao et al. (1989) and Tao and Simpson (1993). The fluxes of momentum, heat, and moisture from the surface are determined according to bulk aerodynamic drag laws. The drag coefficients are prognosed according to Louis et al. (1982) for stable condi-

*Corresponding author address: Jeffrey Frame, Department of Meteorology, Pennsylvania State University, 503 Walker Building, University Park, PA 16802; *e-mail*: jwf155@psu.edu

tions and Byun (1990) for unstable conditions. The turbulence scheme uses a 1.5 order turbulent kinetic energy (TKE) closure and is anisotropic, owing to the relatively fine vertical resolution near the surface when compared with the horizontal resolution. The soil model is based on the two-layer force-restore scheme described by Noilhan and Planton (1989). The NASA Goddard Cumulus Ensemble radiative transfer model was used for both shortwave (Chou 1990, 1992; Chou et al. 1998) and longwave (Tao et al. 1996; Chou et al. 1999) radiation. This model allows for the absorption, scattering, and emission of radiation by atmospheric constituents, including clouds and gases.

Most mesoscale models compute solar radiative transfer with the independent column approximation (ICA), which allows for only the vertical propagation of radiation (Meador and Weaver 1980). In the ICA, all vertical model columns are assumed to be plane-parallel with infinite horizontal extent. Thus, the transfer of radiation is not permitted between columns (Cahalan et al. 2005). These constraints limit any shadowing effects to surface regions directly beneath clouds. Thus, this method cannot capture the extensions of shaded regions that occur when the local solar zenith angle is much different from zero. The ICA also does not allow for an increase in the net solar flux beneath clouds due to both angular influences on the direct beam and the propagation of diffuse radiation into shaded regions from the sides. O'Hirok and Gautier (2005) found that shortwave surface irradiance errors due to the ICA can reach 500 W m^{-2} near the edges of shaded regions.

The tilted independent pixel approximation, also known as the tilted independent column approximation (TICA), is described by Varnai and Davies (1999). It is similar to the ICA, except that the model columns make an angle with the horizontal plane that is equal to the angle of incidence of the direct solar beam. This method is generally more accurate than the ICA in complex cloud fields (Varnai and Davies 1999). One important caveat is that the TICA does not allow the transfer of radiation between slanted columns by multiple scattering, and thus it does not capture the full three-dimensional nature of atmospheric radiative transfer. Output from both the ICA and the TICA were compared to the results of a Monte Carlo calculation by Frame et al. (2008). It was found that the TICA output matched the Monte Carlo output much more closely than did that from the ICA.

The thermodynamic profile is shown in Fig. 1a and is used to initialize all simulations. This sounding includes a small capping inversion to preclude both the widespread development of secondary convection and the rapid mixing out of the low-level moisture after a few hours of simulated radiative heating. The initial wind profile consists of a semi-circular hodograph shifted relative to the origin such that the simulated storm is approximately stationary. In this wind profile, vertical wind shear is confined to the lowest 6 km and the 0-6 km wind differential is 40 m s^{-1}. The TICA0 simulation contains both shortwave and longwave radiation. In simulation IC0, all forms of radiation are prohibited from interacting with any cloud or precipitation particles. Thus, the cloud does not cast a shadow in that simulation.

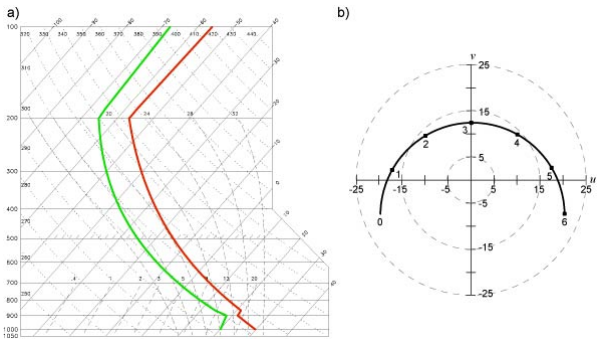

FIG. 1. (a) Skew T-log p diagram depicting the initial temperature (red) and moisture (green) profile. (b) Hodograph depicting the initial wind profile. Winds are shown in m s^{-1}. Speed rings are shown at 5, 15, and 25 m s^{-1}. Elevations are shown at selected points in km.

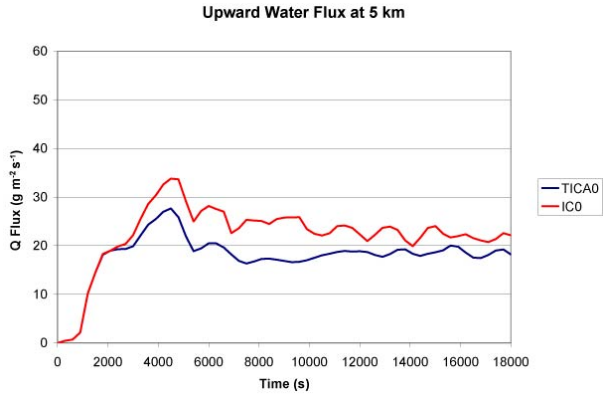

FIG. 2. Total upward water flux at 5 km (g $m^{-2}s^{-1}$) averaged over a 14 $\times$ 14 km box centered on the maximum upward water flux for the TICA0 and IC0 simulations.

3. Results

The time series of the total upward water flux from the TICA0 and IC0 simulations (Fig. 2) reveal that the storm within the IC0 simulation has an upward water flux that is consistently 20-30% greater than that from the TICA0 simulation. When compared to other simulations (not shown), it is evident that the surface shadow has a larger influence on supercell intensity than either longwave radiation or the use of the ICA instead of the TICA. The behavior of the time series of upward water flux is matched by similar time series of maximum updraft intensity (not shown). The water flux metric was chosen in lieu of maximum updraft speed because the water flux accounts for both the intensity and size of the updraft, while the maximum updraft speed only accounts for the former.

The time series of maximum low-level vertical vorticity (Fig. 3) indicates that the storm within the IC0 simulation produces a stronger low-level mesocyclone than does that in the TICA0 simulation. The two vorticity time series exhibit a degree of correlation, especially for about the first three hours of the simulations. For example, there is a maximum in both time series around 6000 s, followed by a minimum around 8000 s. These local maxima and minima become more out of phase as simulation time increases, as one would expect from the chaotic

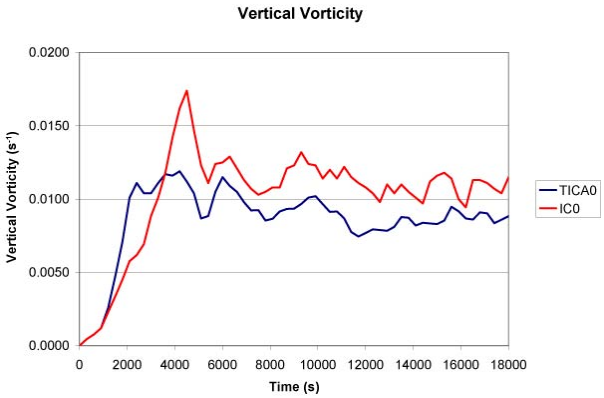

FIG. 3. Maximum vertical vorticity (s^{-1}) in the lowest 500 m for the TICA0 and IC0 simulations.

nature of the atmosphere.

The low-level rainwater, potential temperature, wind, and vertical vorticity fields, along with the midlevel vertical velocity field for the TICA0 and IC0 simulations (Fig. 4) illustrate that the storm in the IC0 simulation evolves much more differently than does the storm in the TICA0 simulation. A large mass of cooler air exists beneath the anvil in the TICA0 simulation. Also, the rear-flank gust front has undercut the updraft and low-level mesocyclone in that simulation, depriving the storm of warm and moist inflow. This weakens the updraft and ultimately leads to a weaker mesocyclone because of reduced vortex stretching beneath the updraft. The storm in the TICA0 simulation exhibits this quasi-steady behavior after about the first 1.5 h of simulation time. It is unknown as to why a secondary updraft does not develop along the rear-flank gust front at a later time; why some individual simulated and observed storms cycle while others do not remains poorly understood. The precipitation core of the IC0 storm, along with the mesocyclone and updraft, are much closer to the warm and moist inflow air in the IC0 simulation than in the TICA0 simulation. This is consistent with a stronger and more intense thunderstorm. The precipitation core in the IC0 simulation is more intense than is that in the TICA0 simulation, which agrees with the greater upward water flux from the IC0 simulation as seen in the time series (Fig. 2). The low-level mesocyclone and the midlevel updraft are also broader in the IC0 simulation, and this is also consistent with the time series discussed above. Additionally, the temperature deficit beneath the anvil is absent after 3 h of simulation time in the IC0 simulation, which is expected given the design of that simulation.

Also notable is a decrease in the surface wind speeds beneath the anvil in the TICA0 simulation. These lessened near-surface wind speeds owe their existence to the radiative cooling of the model surface beneath the anvil. This cooling changes the sign of the surface sensible heat flux beneath the anvil, meaning that the surface cools the boundary layer from below. The cooling of the bottom of a layer of air is a stabilizing effect; it suppresses vertical turbulent mixing as seen through the model turbulent kinetic energy (TKE) field (Fig. 5). This suppression of vertical mixing prevents both the higher momentum air aloft from mixing down to the near-surface layer, and the lower momentum air near the surface from mixing upward and decelerating the flow higher in the model atmosphere.

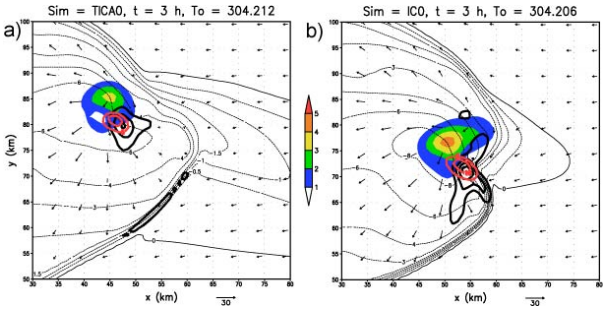

FIG. 4. Rainwater mixing ratio (shaded; g kg^{-1}), potential temperature perturbation (light contour; K), wind vectors (vectors) at 25 m, vertical vorticity at 125 m (thick black contours), and vertical velocity at 2000 m (thick red contours) after 3 h of simulation time for the (a) TICA0 simulation and (b) IC0 simulation. Potential temperature perturbation is taken from an area far from the storm and is as indicated. Irregular potential temperature perturbation contours are 0.0, -0.5, -1.0, -1.5, -2.0, -3.0, -4.0, -6.0, and -8.0 K. Vertical vorticity contour interval is 0.0025 s^{-1}. Vertical velocity contour interval is 5 m s^{-1}, beginning at 5 m s^{-1}. Wind vectors are scaled as indicated.

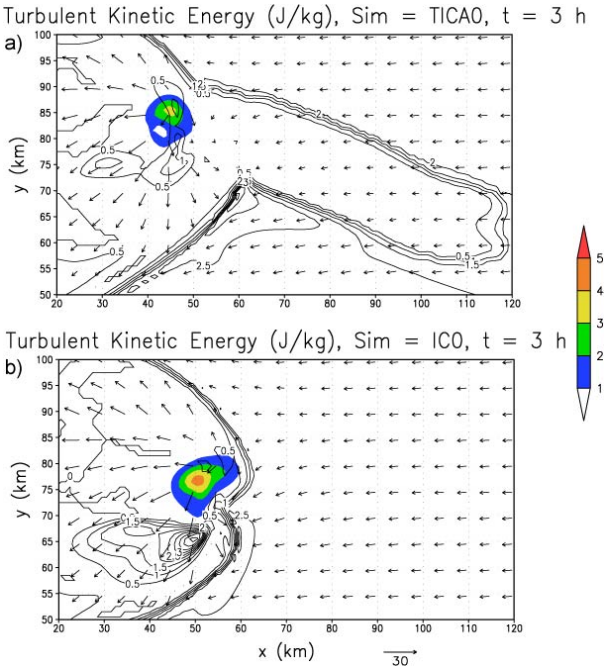

FIG. 5. Turbulent kinetic energy (J kg^{-1}) at 300 m, (contoured) and rainwater mixing ratio (g kg^{-1}, shaded) after 3 h of simulation time for the (a) TICA0 simulation and (b) IC0 simulation. Wind vectors at 25 m are also plotted and scaled as indicated. Contour interval is 0.5 J kg^{-1}.

The different vertical mixing profiles between the full sun and the anvil shadow in the TICA0 simulation result in different vertical shear profiles beneath the anvil in the TICA0 and IC0 simulations. This is readily apparent in east-west vertical cross-sections taken 5 km south of the maximum updraft (Fig. 6). The surface winds beneath the anvil in the TICA0 simulation (east of x = 65 km in Fig. 6a) are much less than those in the IC0 simulation in this same region (Fig. 6b). As

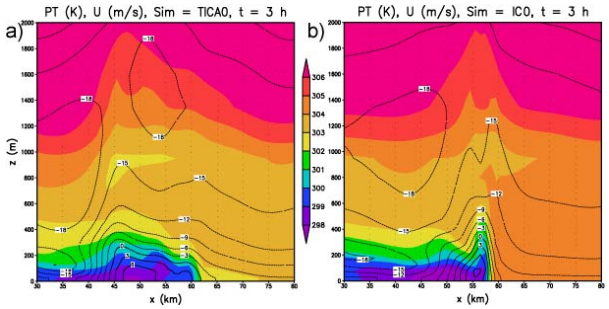

FIG. 6. Vertical east-west cross-section of potential temperature (shaded; K) and zonal wind speed (contoured; m s^{-1}) after 3 h of simulation time for the (a) TICA0 and (b) IC0 simulations. Cross section is taken 5 km south of the maximum updraft at 2000 m in both simulations. Contour interval is 3 m s^{-1}.

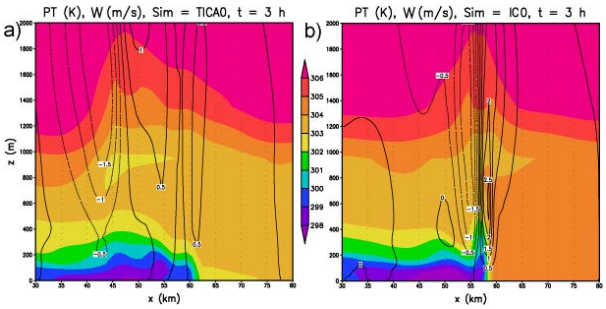

FIG. 7. Vertical east-west cross-section of potential temperature (shaded; K) and vertical velocity (contoured; m s^{-1}) after 3 h of simulation time for the (a) TICA0 and (b) IC0 simulations. Cross section is taken 5 km south of the maximum updraft at 2000 m in both simulations. Contour interval is 0.5 m s^{-1}.

a result of the reduced vertical mixing beneath the anvil in the TICA0 simulation, there is greater vertical wind shear beneath the anvil in that simulation, especially in the lowest 200-300 m of the domain.

Previous simulations of idealized density currents (e.g., Xu et al. 1996) have shown that a density current which moves upshear into a strongly vertically-sheared flow develops a shallow head, which generates much less lift than does a deep density current head (e.g., Xue 2000). A vertical cross-section of vertical velocity (Fig. 7), taken along the same plane as Fig. 6, depicts reduced lift at the cold pool head in the TICA0 simulation. The cold pool also has a shallower head in that simulation, resulting in a weaker updraft that slopes back over the cold pool. Numerical simulations of squall lines (e.g., Weisman et al. 1988) have indicated that updrafts which slope rearward over a cold pool are not as intense as erect updrafts because of increased entrainment of cold air and less proximity to the potentially warm and moist inflow. Although density current dynamics have not been a major focus of previous supercell research, there are numerous anecdotal observations that supercells must possess a balance between cold pool intensity (i.e., the amount of precipitation and the location of the precipitation relative to the updraft) and low-level wind shear in order to remain long lived. If too much cold air builds up beneath the storm, the gust front surges outward, possibly undercutting the updraft and low-level mesocyclone. This is likely similar to the inflow-outflow balance hypothesized in recent observational studies (e.g., Trapp 1999; Wakimoto and Cai 2000; Dowell and Bluestein 2002b; French et al. 2008) of cyclic mesocyclogenesis. Thus, for the environmental wind profile given in Fig. 1, radiation acts to create a weaker storm because the reduced vertical mixing beneath the anvil allows the rear-flank gust front to surge eastward and undercut the low-level updraft and mesocyclone.

4. Conclusions

The inclusion of radiation led to important modifications to the near-storm environment via the anvil shadow. The reduced solar flux within the shaded region cooled surface temperatures and this cooling was transferred to the air by the surface sensible heat flux. This cooling stabilized the boundary layer and suppressed vertical mixing, as seen through the turbulent kinetic energy fields. The loss of boundary layer vertical mixing prevented air from near the surface, which had lost momentum to friction, from mixing with higher momentum air from aloft. This process increased the magnitude of the near-surface vertical wind shear beneath the anvil, and allowed the rear-flank gust front to become shallower and accelerate in the anvil-shaded region. In the case of the approximately stationary thunderstorm examined herein, the cold outflow was able to wrap around the mesocyclone and undercut the updraft. Both of these processes deprived the supercell of warm, potentially buoyant air and weakened it as seen in simulation TICA0. This process is shown schematically in Fig. 8a. If the anvil shading was not considered in the numerical model as in simulation IC0 (Fig. 8b), these processes did not occur and the stationary storm was more intense.

These results cannot be generalized to all simulations of supercells. Subsequent simulations have recorded that changing the ground-relative wind profile yields different storm motions relative to the orientation of anvil in the presence of surface friction. These simulations demonstrated that the above processes is only active if the rear-flank gust front propagates into the shadowed region. It is likely that changing environmental conditions, especially the storm-relative wind profile, may impact the results described herein. Low-precipitation supercells, for example, may be less sensitive to the interaction between the gust front and the ambient vertical wind shear. Additionally, it is possible that different microphysical parameterizations, which affect outflow temperatures, can influence these results. The influences radiation on other convective modes, such as squall lines and ordinary thunderstorms should be investigated as well. It is possible that similar modifications of the low-level shear beneath the anvil of a squall line could help rectify the differences in optimal shear values between observed (e.g., Evans and Doswell 2001) and simulated (e.g., Weisman and Rotunno 2004) squall lines. Future simulations and observations should also investigate the hypothetical balance between a supercell's inflow and its outflow, which is believed to differentiate between a storm possessing a single long-lived mesocyclone and one which undergoes cyclic mesocyclogenesis.

Acknowledgments. We wish to thank Drs. Yvette Richardson, Jerry Harrington, Bill Frank, and Andrew Carleton for their constructive comments. Conversations with Drs. Eugene Clothiaux and Tamas Varnai improved the adoption of TICA

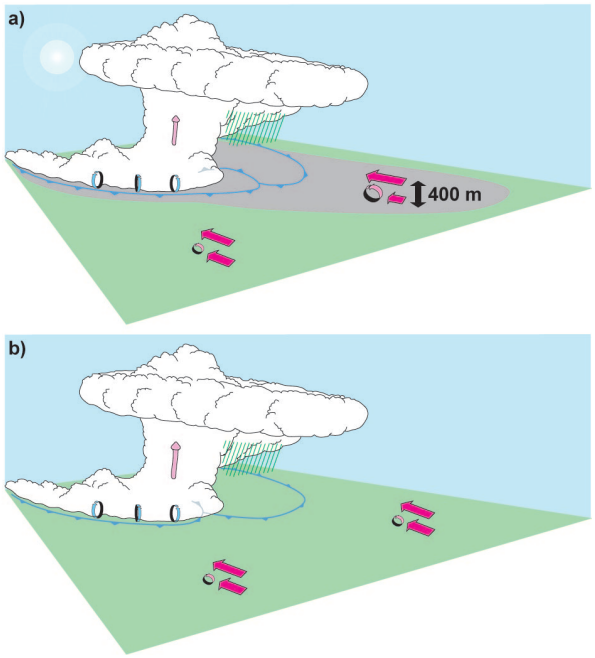

FIG. 8. Schematic diagram illustrating how anvil shading affects the propagation of the rear-flank gust front and storm intensity. (a) If anvil shading is considered, the near-surface winds in the shadowed region weaken owing to surface drag and the corresponding loss of vertical mixing, allowing the gust front to propagate far in front of the storm. A weaker storm results. (b) Without anvil shading, the gust front is restrained and the storm is stronger. Solid pink arrows represent horizontal wind vectors at different levels and light pink arrows represent updrafts. Size of arrows represents strength of flow. The gust front is denoted by conventional notation. Horizontal vorticity is also shown. The area shaded by the anvil is indicated.

for use within ARPS. Assistance from Chad Bahrmann, Rob Carver, Kent Knopfmeier, Mario Majcen, Jim Marquis, and Dr. Chuck Pavloski is also acknowledged. ARPS is a product of the Center for Analysis and Prediction of Storms at the University of Oklahoma. All cross-sectional figures shown were produced using GrADS software. This work was funded by NSF grants ATM-0338661, ATM-0437512, and ATM-0644533.

REFERENCES

Brooks, H. E., C. A. Doswell III, and J. Cooper, 1994: On the environments of tornadic and nontornadic mesocyclones. *Wea. Forecasting*, **9**, 606–618.

Byun, D. W., 1990: On the analytical solutions of flux-profile relationships for the atmospheric surface layer. *J. Appl. Meteor.*, **29**, 652–657.

Cahalan, R. F. and Coauthors, 2005: The I3RC: Bringing together the most advanced radiative transfer tools for cloudy atmospheres. *Bull. Amer. Meteor. Soc.*, **86**, 1275–1293.

Chin, H.-N. S, 1994: The impact of the ice phase and radiation on a midlatitude squall line system. *J. Atmos. Sci.*, **51**, 3320–3343.

Chou, M.-D., 1990: Parameterizations for the absorption of solar radiation by O_2 and CO_2 with application to climate studies. *J. Climate*, **3**, 209–217.

Chou, M.-D., 1992: A solar radiation model for use in climate studies. *J. Atmos. Sci.*, **49**, 762–772.

Chou, M.-D., K.-T. Lee, S.-C. Tsay, and Q. Fu, 1999: Parameterization for cloud longwave scattering for use in atmospheric models. *J. Climate*, **12**, 159–169.

Chou, M.-D., M. J. Suarez, C.-H. Ho, M. M.-H. Yan, and K.-T. Lee, 1998: Parameterizations for cloud overlapping and shortwave single-scattering properties for use in general circulation and cloud ensemble models. *J. Climate*, **11**, 202–214.

Dowell, D. C. and H. B. Bluestein, 1997: The Arcadia, Oklahoma, storm on 17 May 1981: Analysis of a supercell during tornadogenesis. *Mon. Wea. Rev.*, **125**, 2562–2582.

Dowell, D. C. and H. B. Bluestein, 2002: The 8 June 1995 McLean, Texas, storm. Part II: Cyclic tornado formation, maintenance, and dissipation. *Mon. Wea. Rev.*, **130**, 2649–2670.

Evans, J. S. and C. A. Doswell, III, 2001: Examination of derecho environments using proximity soundings. *Wea. Forecasting*, **16**, 329–342.

Finley, C. A., W. R. Cotton, and R. A. Pielke, Sr., 2001: Numerical simulation of tornadogenesis in a high-precipitation supercell. Part I: Storm evolution and transition into a bow echo. *J. Atmos. Sci.*, **58**, 1597–1629.

Frame, J. W., J. L. Petters, P. M. Markowski, and J. Y. Harrington, 2008: An application of the tilted independent pixel approximation to cumulonimbus environments. *Atmos. Res.*, in press.

French, M. M., H. B. Bluestein, D. C. Dowell, L. J. Wicker, M. R. Kramar, and A. L. Pazmany, 2008: High-resolution, mobile Doppler radar observations of cyclic mesocyclogenesis in a supercell. *Mon. Wea. Rev.*, in press.

Kelly, J. L., J. T. Schaefer, R. P. McNulty, C. A. Doswell III, and R. F. Abbey, Jr, 1978: An augmented tornado climatology. *Mon. Wea. Rev.*, **106**, 1172–1183.

Kessler, E., 1969: *On the Distribution and Continuity of Water-Substance in Atmospheric Circulations. Meteor. Monogr.*, No. 32, Amer. Meteor. Soc., 84 pp.

Khairoutdinov, M. F. and D. A. Randall, 2002: Similarity of deep continental cumulus convection as revealed by a three-dimensional cloud-resolving model. *J. Atmos. Sci.*, **59**, 2550–2566.

Khairoutdinov, M. F. and D. A. Randall, 2003: Cloud resolving modeling of the ARM Summer 1997 IOP: Model formulation, results, uncertainties, and sensitivities. *J. Atmos. Sci.*, **60**, 607–625.

Lin, Y.-L., R. D. Farley, and H. D. Orville, 1983: Bulk parameterization of the snow field in a cloud model. *J. Appl. Meteor.*, **22**, 1065–1092.

Louis, J. F., M. Tiedtke, and J. F. Geleyn, 1982: A short history of the operational PBL parameterization at ECMWF. *ECMWF Workshop on Planetary Boundary Parameterizations*, Nov., 1981, 59-79.

Markowski, P. M. and J. Y. Harrington, 2005: A simulation of a supercell thunderstorm with emulated radiative cooling beneath the anvil. *J. Atmos. Sci.*, **62**, 2607–2617.

Markowski, P. M., E. N. Rasmussen, J. M. Straka, and D. C. Dowell, 1998: Observations of low-level baroclinity generated by anvil shadows. *Mon. Wea. Rev.*, **126**, 2942–2958.

Meador, W. E. and W. R Weaver, 1980: Two-stream approximations to radiative transfer in planetary atmospheres: A valid description of existing relations and a new improvement. *J. Atmos. Sci.*, **37**, 630–643.

Miller, R. A. and W. M. Frank, 1993: Radiative forcing of simulated tropical cloud clusters. *Mon. Wea. Rev.*, **121**, 482–498.

Noilhan, J. and S. Planton, 1989: A simple parameterization of land surface processes for meteorological models. *Mon. Wea. Rev.*, **117**, 536–549.

O'Hirok, W. and C. Gautier, 2005: The impact of model resolution on differences between independent column approximation and Monte Carlo estimates of shortwave surface irradiance and atmospheric heating rate. *J. Atmos. Sci.*, **62**, 2939–2951.

Orlanski, I., 1976: A simple boundary condition for unbounded hyperbolic flows. *J. Comput. Phys.*, **21**, 251–269.

Tao, W.-K., S. Lang, J. Simpson, C.-H. Sui, B. Ferrier, and M.-D. Chou, 1996: Mechanisms of cloud-radiation interaction in the Tropics and Midlatitudes. *J. Atmos. Sci.*, **53**, 2624–2651.

Tao, W.-K. and J. Simpson, 1993: The Goddard Cumulus Ensemble model. Part I: Model description. *Terr. Atmos. Oceanic Sci.*, **4**, 35–72.

Tao, W.-K., J. Simpson, and M. McCumber, 1989: An ice-water saturation adjustment. *Mon. Wea. Rev.*, **117**, 231–235.

Trapp, R. J., 1999: Observations of nontornadic low-level mesocyclones and attendant tornadogenesis failure during VORTEX. *Mon. Wea. Rev.*, **127**, 1693–1705.

Trier, S. B., M. A. LeMone, and W. C. Skamarock, 1998: Effect of three dimensional structure on the stormwide horizontal accelerations and momentum budget of a simulated squall line. *Mon. Wea. Rev.*, **126**, 2580–2598.

Trier, S. B., W. C. Skamarock, and M. A. LeMone, 1997: Structure and evolution of the 22 February 1993 TOGA COARE squall line: Organization mechanisms inferred from numerical simulation. *J. Atmos. Sci.*, **54**, 386–407.

Varnai, T. and R. Davies, 1999: Effects of cloud heterogeneities on shortwave radiation: Comparison of cloud-top variability and internal heterogeneity. *J. Atmos. Sci.*, **56**, 4206–4224.

Wakimoto, R. M. and H. Cai, 2000: Analysis of a nontornadic storm during VORTEX 95. *Mon. Wea. Rev.*, **128**, 565–592.

Weisman, M. L., J. B. Klemp, and R. Rotunno, 1988: Structure and evolution of numerically simulated squall lines. *J. Atmos. Sci.*, **45**, 1990–2013.

Weisman, M. L. and R. Rotunno, 2004: "A theory for strong, long-lived squall lines" revisited. *J. Atmos. Sci.* , **61**, 361–382.

Xu, K.-M. and D. A. Randall, 1995: Impact of interactive radiative transfer on the macroscopic behavior of cumulus ensembles. Part I: Radiation parameterization and sensitivity tests. *J. Atmos. Sci.* , **52**, 785–799.

Xu, Q., M. Xue, and K. K. Droegemeier, 1996: Numerical simulations of density currents in sheared environments within a vertically confined channel. *J. Atmos. Sci.*, **53**, 770–786.

Xue, M., 2000: Density currents in two-layer shear flows. *Quart. J. Roy. Meteor. Soc.*, **126**, 1301–1320.

Xue, M., K. K. Droegemeier and V. Wong, 2000: The Advanced Regional Prediction System (ARPS): A multiscale nonhydrostatic atmospheric simulation and prediction tool. Part I: Model dynamics and verification. *Meteor. Atmos. Phys.*, **75**, 161–193.

Xue, M., K. K. Droegemeier, V. Wong, A. Shapiro, K. Brewster, F. Carr, D. Weber, Y. Liu and D. H. Wang, 2001: The Advanced Regional Prediction System (ARPS): A multiscale nonhydrostatic atmospheric simulation and prediction tool. Part II: Model physics and applications. *Meteor. Atmos. Phys.*, **76**, 143–165.